Materials Horizons

ROYAL SOCIETY OF CHEMISTRY

COMMUNICATION

View Article Online
View Journal | View Issue

Cite this: *Mater. Horiz.*, 2026, **13**, 1056

Received 8th September 2025,
Accepted 15th October 2025

DOI: 10.1039/d5mh01710f

rsc.li/materials-horizons

Persistent radicals in organic photonic synaptic transistors for pattern recognition of electrical and multicolor optical stimuli

Giulia Baroni,†[a] Francesco Reginato,†[a] Ugo Bruno,†‡[d] Francesco Porcelli,[b] Giuseppe Mattioli,[b] Sara Mattiello,[c] Luca Beverina,[c] Mario Prosa,[a] Margherita Bolognesi,[a] Francesca Santoro *[e] and Stefano Toffanin *[a]

Organic photonic synaptic transistors (OPSTs) integrate light detection and signal processing, memory, and computation capabilities due to their intrinsic multifunctionality. Despite the many strategies reported in the literature, OPSTs mainly rely on nanomaterial engineering, while a true molecular design approach to the intrinsic properties of the materials, enabling a finer control of neuromorphic functions, is still lacking. This study presents a solution-processed multilayer OPST, integrating in a single device the functions of multi-modal synapsis and dendritic-like neuromorphic computing. The device combines a bulk heterojunction photoactive layer based on a persistent organic radical and a relaxor-like ferroelectric polymer as a dielectric layer. Multilevel atomistic simulations illustrate how the peculiar electronic structure of the persistent organic radical in the photoactive layer enables the activation of different photophysical pathways occurring under different (multicolor) optical stimulations, which can correlate with different synaptic outputs (current facilitation) in the device. Then, we first show experimentally that synaptic functions such as short-term and long-term plasticity (STP and LTP, respectively) are enabled in the OPST by the synergic combination of optical and electrical stimulations: STP under blue-light stimulation and LTP under near-infrared light-stimulation or under sequential blue-light and electrical stimulation. Then, we demonstrate that the multi-mode operation of the OPST allows modulating a neuromorphic behavior which simulates dendritic parallel learning and signal integration under different patterns of the incoming stimuli. Specifically, different patterns from eight combinations of optical and electrical stimuli are recognized and classified. Overall, the proposed material-design based approach lays the foundation for a new class of organic photonic synaptic devices, including OPSTs, that can perform complex dendritic computations, paving the way for more efficient and powerful artificial photonic neural systems.

New concepts

We present an innovative solution-processed organic photonic synaptic transistor (OPST) designed as a multiple-stimuli synaptic device by implementing for the first time a persistent organic radical capable of multiple wavelength photoexcitation in the photoactive layer and a ferroelectric polymer as the dielectric layer that exhibits electrically induced polarization. In the literature, multiple and uncorrelated strategies can be used to achieve memory characteristics by photo-inducing trapping sites in the different functional layers of OPSTs. However, none of them are grounded in a purely molecular engineering and chemical design approach of constituent materials. Instead, the methodologies reported so far predominantly rely on trial-and-error engineering of nanomaterials, in terms of structural, morphological, and compositional optimization at the nanoscale. In this work, we demonstrate by means of theoretical calculations that the long-term memory is enabled by the formation of specific trap states in the radical component of the photoactive layer of the OPST, thus clearly correlating the molecular electronic configuration and neuromorphic properties in such prototypal organic compounds. We exploit the intrinsic multifunctionality of an OPST based on a persistent radical for emulating dendrite integration which is a neuromorphic feature rarely explored but fundamental to perform spatio-temporal pattern discrimination and network-level computation (*i.e.* for artificial retina applications).

[a] *Istituto per lo Studio dei Materiali Nanostrutturati (ISMN), Consiglio Nazionale delle Ricerche (CNR), Via P. Gobetti 101, 40129, Bologna, Italy. E-mail: stefano.toffanin@cnr.it*
[b] *Istituto di Struttura della Materia (ISM), Consiglio Nazionale delle Ricerche (CNR), Via Salaria Km 29.5, 00016, Monterotondo Stazione, Italy*
[c] *Dipartimento di Scienza dei Materiali, Università di Milano Bicocca, Piazza dell'Ateneo Nuovo 1, 20126, Milano, Italy*
[d] *Laboratory of Organic Electronics, Department of Science and Technology, Linköping University, Bredgatan 33, 602 21 Norrköping, Sweden*
[e] *Fakultät für Elektrotechnik und Informationstechnik, RWTH Aachen University, Sommerfeldstrasse 18, Turm 24, 52074, Aachen, Germany. E-mail: f.santoro@fz-juelich.de*
† These authors contributed equally to the work.
‡ U. Bruno previously held a position at Tissue Electronics, Istituto Italiano di Tecnologia, Dipartimento di Chimica, Materiali e Produzione Industriale, Università di Napoli Federico II, Naples, 80125, Italy.

Introduction

Neuromorphic engineering involves fabrication of electronic devices that are able to mimic the nonlinear and parallel characteristics of the biological neural system, therefore implementing brain-inspired computing.[1] Great efforts have been made to design and fabricate electronic devices that emulate synapses by varying device architecture and active materials and collecting different physical observables.[2–6] It is expected that these innovative optical, electrical and optoelectronic devices, capable of emulating brain functions, will lead to the foundation of a novel generation of hardware by combining energy efficiency with multiple computational capabilities,[7] such as colocalization of memory and processing, pattern recognition in time and space, non-volatile memory retention and autonomous adaptation in response to external stimuli.[8–13]

Such features are enabled by mimicking the processing and propagation of information in neural cells which are based on the release and binding of neurotransmitters between pre- and post-synaptic neurons with consequent recording of the excitatory/inhibitory post-synaptic currents (EPSC/IPSC) at the post-synaptic neuron.[14] In addition, the strength of the synaptic communication, *i.e.*, synaptic weight, is dynamically adjusted, resulting in neuroplasticity[15] that is classified as short-term or long-term plasticity (STP/LTP) according to the timescale of the mechanism.[16–18]

In this context, synaptic devices based on transistors are garnering interest, thanks to the possibility to modulate the channel conductance acting on the pre-synaptic gate electrode, resulting in neuroplastic characteristics in the drain current (post-synaptic output).[2,19,20] Since signal transmission and self-learning can be performed simultaneously, transistor architectures are especially well-suited to simulate parallel learning and dendrite integration.[21–23] Despite the widest endeavor of neuromorphic engineering being devoted to the emulation of neural features such as spiking signaling,[24,25] colocalization of memory and computation,[26,27] synaptic plasticity,[28,29] and energy efficiency,[30] dendritic computing is gaining more and more attention.[31] Dendrites actively occupy up to 50% of the total membrane volume in neuronal cells, accounting for several computational functions, spanning from simple Boolean operations (AND, OR, and NOT),[32] to the possibility to perform spatio-temporal pattern discrimination and network-level computation, as in the case of dendritic spines.[33,34] For instance, a prominent example of dendritic pattern recognition can be found in the retina. Here, the information related to the direction of motion is mainly encoded within the dendritic signaling of starburst amacrine cells and direction-selective ganglion cells.[35,36]

The capability of interacting with light is mandatory not only for generating retina-inspired artificial visual systems (AVSs) but also for optogenetics, photonic neuromorphic systems and optical computing. In this regard, organic photonic synaptic transistors (OPSTs) are multifunctional organic field-effect transistors (OFETs) which not only show mechanical flexibility, biocompatibility, and large-area solution processability but also may merge multiple functionalities in a single device which can be independently controlled and exploited.[37–41] This class of devices integrates sensing and memory functions and, compared to two-terminal devices such as diodes, has more signal modulation methods (light stimulation and gate voltage stimulation), higher degrees of freedom on the electrical control (gate voltage regulation), higher signal-to-noise ratio, low crosstalk, and parallel processing.[42]

In OPSTs, the core requirement is that the conductivity of the device can be controlled by light while maintaining memory. The light-induced modulation of the response current in OPSTs, other than by photovoltaic effects, can be related to photoconductive gain and photoinduced polarization, which in turn are all based on charge retention or trapping. Several strategies can be used to achieve memory characteristics by localizing trapping sites in the device structure. These include positioning charge trapping materials like quantum dots, metal nanoparticles, and organic molecules within the semiconducting layers, especially in the bulk heterojunction (BHJ) based photoactive layer,[43–45] at the interface between the semiconducting and dielectric layers,[46] and within the dielectric layer.[47–49] Despite the variety of strategies already present in the literature, none of them are grounded in a purely molecular engineering and chemical design approach of the constituent materials. Instead, the methodologies reported so far predominantly rely on trial-and-error engineering of nanomaterials, in terms of structural, morphological, and compositional optimization at the nanoscale, rather than on the tailoring of photophysical properties at the molecular level. In this view, organic persistent radicals show a peculiar electronic structure displaying a singly unoccupied molecular orbital (SUMO) that allows them to efficiently accept and trap electrons.[50] Compared to closed-shell molecules, organic persistent radicals exhibit doublet electronic ground states and possess a richer landscape of frontier orbitals, which provide the possibility to control the information storage process directly at the molecular level, rather than only by suitable engineering of the BHJ system where they are dispersed. We have recently reported on their use in organic light emitting transistors (OLETs) and organic phototransistors (OPTs) for efficient exciton formation and enhanced photo-gain, respectively.[51,52]

To allow OPSTs to perform neuromorphic functions such as parallel learning and dendrite integration, responsiveness to different input signals simultaneously is preferred. A molecular design-based approach already present in the literature on OPSTs for introducing electrical stimulation is the use of ferroelectric materials as gate dielectrics as they exhibit high polarization, dielectric constant, and capacitance, enabling multilevel channel conductance that creates different memory states, as it is typically done in ferroelectric field–effect transistors (Fe–FETs).[53–55] Among existing polymeric ferroelectric dielectrics, the terpolymer poly(vinylidene fluoride–trifluoroethylene–chlorofluoroethylene) (PVDF–TrFE–CFE) is an excellent candidate to be implemented in emerging synaptic devices thanks to its high stability in the electrically induced and switched polarization states.[56,57]

In this article, we report an all solution-processed OPST that comprises (i) a BHJ photoactive layer, based on a low band-gap polymer as the electron donor, *i.e.* poly(*N*-alkyl diketopyrrolopyrrole dithienylthieno [3,2-*b*]thiophene) (DPP-DTT), and an organic persistent radical (namely the PyPBTM radical) as the electron acceptor[58] and (ii) the ferroelectric PVDF–TrFE–CFE as the dielectric layer. The device presents a multilayer architecture in which the same semiconductor polymer, *i.e.* DPP-DTT, serves as both the hole-transporting layer (HTL) in the transistor channel and the donor in the BHJ-based photoactive layer.[59,60]

The selection of materials in the photoactive and dielectric layers, and the OPST structure itself, provides an innovative device emulating a multiple-stimuli synapse. In the resulting multi-mode OPST, neuromorphic characteristics are demonstrated under electrical stimulation at the gate electrode (electrical synapse) and upon optical stimulation with visible light (optical synapse).

Multilevel atomistic simulations reveal how the transition from STP to LTP arises from distinct photophysical processes in the BHJ, each triggered by specific light wavelengths and involving different molecular energy/spin states of the PyPBTM radical. Accordingly, the neuroplasticity in OPSTs is modulated by the light-excitation wavelength: while only STP is emulated by blue light excitation, both STP and LTP characteristics are recorded under near infrared (NIR) light.

Different combinations of sequential electrical and optical stimuli are applied to the OPST, which is demonstrated to operate with a nonlinear integration of inputs. Eventually, electro–optical pattern recognition is achieved, emulating a dendrite spatio-temporal integration of the incoming stimuli. Collectively, our findings demonstrate the possible use of the multi-mode OPST in artificial photonic neural systems, including AVS-related applications like image classification, facial recognition, autonomous driving, and security monitoring.[42]

Results and discussion

Fig. 1a shows the cross-sectional view of the solution-processed bilayer OPST with a bottom-gate/middle-contact configuration presented in this work. A patterned ITO glass serves as the transparent gate contact, while silver source/drain electrodes are embedded between the DPP-DTT hole-transporting layer (HTL) and the photoactive BHJ, which consists of a blend of DPP-DTT and PyPBTM. The DPP-DTT in the HTL is crosslinked by 1,6-bis(trichlorosilyl)hexane (C6Si) in order to guarantee solvent orthogonality with respect to the DPP-DTT based BHJ layer and to preserve high hole mobility (up to 1 $cm^2 V^{-1} s^{-1}$) in field-effect transistors.[40,59,60] The chemical structures of the active materials and dielectric polymer PVDF–TrFE–CFE are shown in Fig. 1b.

The absorption spectrum of the BHJ obtained by blending DPP-DTT and PyPBTM in the 1 : 3 weight ratio highlights that the photoactive layer can be excited in three different

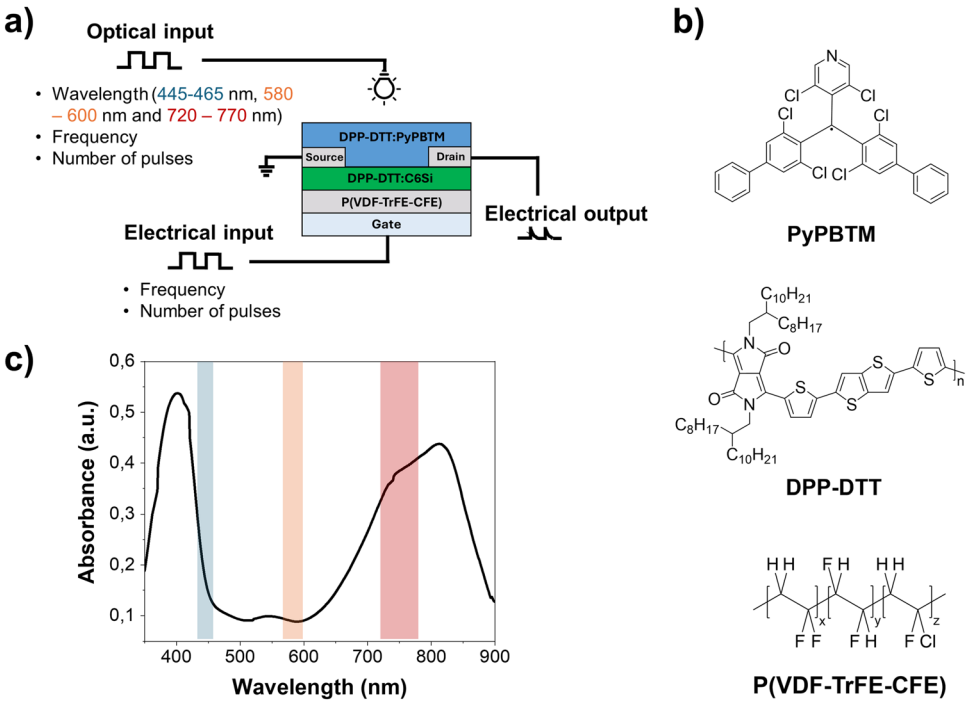

Fig. 1 (a) Cross-sectional view of the multi-mode OPST for simulating biological synapse under electrical and optical stimulations. (b) Molecular structures of the organic persistent radical PyPBTM used as the electron acceptor in the BHJ photoactive layer of the OPST, of the DPP-DTT polymer used as both the electron donor in the BHJ photoactive layer and as the HTL in the OPST and of the PVDF–TrFE–CFE ferroelectric polymer used as the dielectric in the OPST. (c) Absorption spectrum of the DPP-DTT-PyPBTM 1 : 3 thin film used as the BHJ photoactive layer in the OPST, with indication of the three spectral regions corresponding to the optical excitation in the blue, yellow and near infrared regions.

wavelength ranges corresponding to the relative maxima in the absorption spectra located at around 400 nm (blue light), 550 nm (yellow light) and 820 nm (NIR light). This specific composition of the BHJ has been previously identified in OPTs showing enhanced photosensitivity under NIR excitation.[52]

Time-dependent density functional theory (TDDFT) calculations were performed on the PyPBTM:DPP-DTT system. As reported in our previous works,[51,58] and consistent with the PyBTM series, the α-highest occupied molecular orbital (α-HOMO) and the β-HOMO form an almost degenerate pair, with both orbitals primarily localized on the peripheral substituents (Fig. S1a). The singly occupied and unoccupied molecular orbitals (α-SOMO and β-SUMO, respectively) are primarily localized on the central carbon atom, while the lowest unoccupied molecular orbital (LUMO) and LUMO+1 are predominantly localized on the di-Cl-pyridine moiety, which serves as the electron-accepting component, and on the di-Cl-benzene groups, respectively. The TDDFT absorption spectrum of PyPBTM (Fig. S1b) is in good agreement with the correlated portion of the experimental absorption spectrum of the photoactive BHJ layer shown in Fig. 1c: the sharp band peaked at 412 nm (corresponding to blue light excitation) is a convolution of the two degenerate α-SOMO → α-LUMO and α-SOMO → α-LUMO+1 transitions, while the weaker and broader band at 548 nm (yellow light excitation), corresponding to the doublet $D_0 \rightarrow D_1$ transition, is assigned to the transition from the β-HOMO to the β-SUMO. On the other hand, NIR irradiation at 770 nm of the photoactive BHJ layer selectively excites the polymer from its ground to its first excited singlet states: accordingly, theoretical calculations considering a DPP-DTT tetramer indicate this transition at 706 nm (see the Experimental section for more details).

As a result of the complex energy landscape of the photoactive BHJ system, multiple paths comprising different photophysical processes can take place, depending on whether the generation of excitons occurs in the DPP-DTT or PyPBTM domains of the BHJ and on which optical transition in PyPBTM is involved. While the path and fate for minority carriers (electrons) are different from case to case, majority carriers (holes) formed in the BHJ layer can be isoenergetically transferred to the bottom HTL and contribute to the channel current, in all foreseen pathways.

We quantified the capability of the OPSTs to respond to different continuous light stimuli by collecting the transfer curve characteristics, which is a measure of the source-drain current (I_{ds}) during a sweep of the source-gate voltage (V_{gs}) at a fixed source-drain voltage (V_{ds}), in the dark and under different illumination conditions: (i) at different excitation wavelengths and (ii) at different values of illumination optical power density (Fig. S2). The best photosensitivity (P) of the OPST, calculated from the transfer characteristics reported in Fig. S2, is observed at the maximum illumination power density of 1.6 mW cm^{-2}. P values of 6.6×10^5, 5.4×10^4 and 4.5×10^5 are obtained for illumination in the blue (445–465 nm), yellow (580–600 nm) and NIR ranges (720–770 nm), respectively. Such P values are in agreement with the best performing solution processed OPTs reported in the literature.[52] The similar P values in the blue and NIR ranges, and the lower value in the yellow range, perfectly reflect the absorption spectrum of the BHJ layer (Fig. 1c).

In the multi-mode OPST, the channel current measured at the drain, *i.e.* the post-synaptic signal, can be modulated by supplying multiple pre-synaptic inputs as gate-source voltage (V_{gs}) pulses, as it is typically done in Fe–FETs endowed with ferroelectric dielectrics, and multiple-wavelength optical excitation pulses at the photoactive layer.

To identify the contribution to the modulation of the conductivity of the channel due to the electrically induced polarization of the ferroelectric dielectric in OPSTs, Fe–FETs were used as test devices consisting only of PVDF–TrFE–CFE as the dielectric layer and the cross-linked DPP-DTT as the HTL (Fig. S3a). The transfer curve characteristics under p-type polarization, shown in Fig. S3b, exhibit an anticlockwise hysteresis loop of the collected I_{ds}. This results in higher channel current in the backward V_{gs} scan with respect to the forward V_{gs} scan, at the same voltage bias value, reflecting the hysteretic behavior typical of non-volatile information storage devices.[61] Indeed, the transient I_{ds} current of the same Fe–FET, measured under a pulsed electrical stimulation at the gate electrode (pulsed V_{gs} bias from 0 V to −4 V, at a frequency of 0.15 Hz) and normalized at the maximum current collected during the electrical stimulation, increases gradually after each V_{gs} pulse (Fig. 2a). The observed hysteresis of the I_{ds} current during the transfer curve, and the channel-current facilitation behavior under pulsed electrical stimulations, can be explained by the occurrence of a semi-permanent polarization of the PVDF–TrFE–CFE dielectric layer during a forward V_{gs} scan or after a V_{gs} pulse. Overall, under an electrical stimulus (pre-synaptic signal), the I_{ds} channel current increases (post-synaptic signal), thanks to the modulation of polarization of the PVDF–TrFE–CFE ferroelectric dielectric.[21]

The neuromorphic behavior upon electrical-only stimulation in the dark was then studied on the complete OPST. Channel current facilitation was also observed in this case, excluding relevant contributions from the photoactive layer, as it is demonstrated by the collected I_{ds} current increasing in time and normalized at the maximum value during the stimulation (Fig. 2b). Then, the channel current facilitation effect was quantified and optimized by collecting the transient I_{ds} current at different V_{gs} pulse frequencies. The spike-number-dependent plasticity (SNDP) gain, expressed as the percentage ratio between the signal amplitude at the n-th pulse (A_n) and the first one (A_1), was calculated for three tested V_{gs} frequency values (*i.e.* 0.15, 0.5 and 1 Hz as shown in Fig. 2c). As expected, SNDP is greater at the lowest tested V_{gs} frequency (0.15 Hz), reflecting the proposed mechanism of semi-permanent dipole orientation within the PVDF–TrFE–CFE layer, responsible for the current facilitation under electrical-only stimulation in the dark. Notably, A_{100}/A_1 reaches 949% at a V_{gs} pulse frequency of 0.15 Hz, while it decreases to 380% and 309% for frequency values of 0.5 Hz and 1 Hz, respectively.

The neuromorphic behavior of the complete OPST was then tested for optical-only stimulation by applying light pulses in

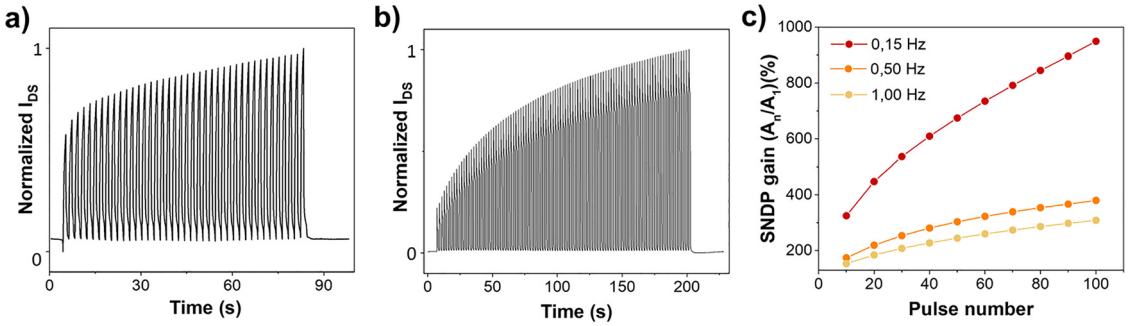

Fig. 2 (a) Normalized I_{ds} current of the reference Fe–FET schematized in Fig. S3a under 40 continuous electrical pulses (V_{gs} = −4 V at a pulse frequency of 0.15 Hz). (b) Normalized I_{ds} current of the OPST under 100 continuous electrical pulses (V_{gs} = −4 V at a pulse frequency of 0.15 Hz). In (a) and (b), the current is normalized at the maximum value collected during the stimulation. (c) SNDP gain (A_n/A_1) (%) *versus* V_{gs} pulse number, measured for the OPST, at different V_{gs} pulse frequency values.

the two different wavelength ranges (blue or NIR) where the OPST shows a greater sensitivity. In order to discriminate between STP and LTP, the paired-pulse facilitation/depression (PPF/PPD), which is the amplitude of EPSC/IPSC triggered by two consecutive pre-synaptic stimuli, is determined. By applying two consecutive identical light pulses in the blue or NIR ranges, the I_{ds} current of the OPST indeed shows PPF characteristics, with the second I_{ds} peak (A_2) having higher intensity than the first one (A_1) (Fig. 3a and b).[62–64]

For both blue and NIR pulsed light stimulations, the OPST device shows stronger learning behavior as the frequency of the optical stimuli increases. However, the PPF index increases much faster in the case of the blue light stimulation as compared to the NIR light stimulation, increasing from 100% to 658% when the frequency is increased only from 0.5 to 1.2 Hz, and increasing from 108.1% to 110.8% when the frequency is increased from 0.15 to 2 Hz, respectively (Fig. 3c and d). Notably, under blue-light excitation, the PPF does not reach a saturation value at the tested frequencies, different from the case of NIR-light excitation. The LTP characteristics of the OPST were investigated under an increasing number of subsequent optical stimulation pulses.

For the pulsed optical stimulation in the blue range (Fig. 3e), the OPST does not show LTP characteristics, since the I_{ds} current returns to the same value shown before the application of the optical stimulation and independent of the number of applied pulses. Instead, for the pulsed stimulation in the NIR range (Fig. 3f), a residual I_{ds} current that is proportional to the number of received optical stimuli is registered after the stimulation protocol ends, thus indicating an LTP effect.

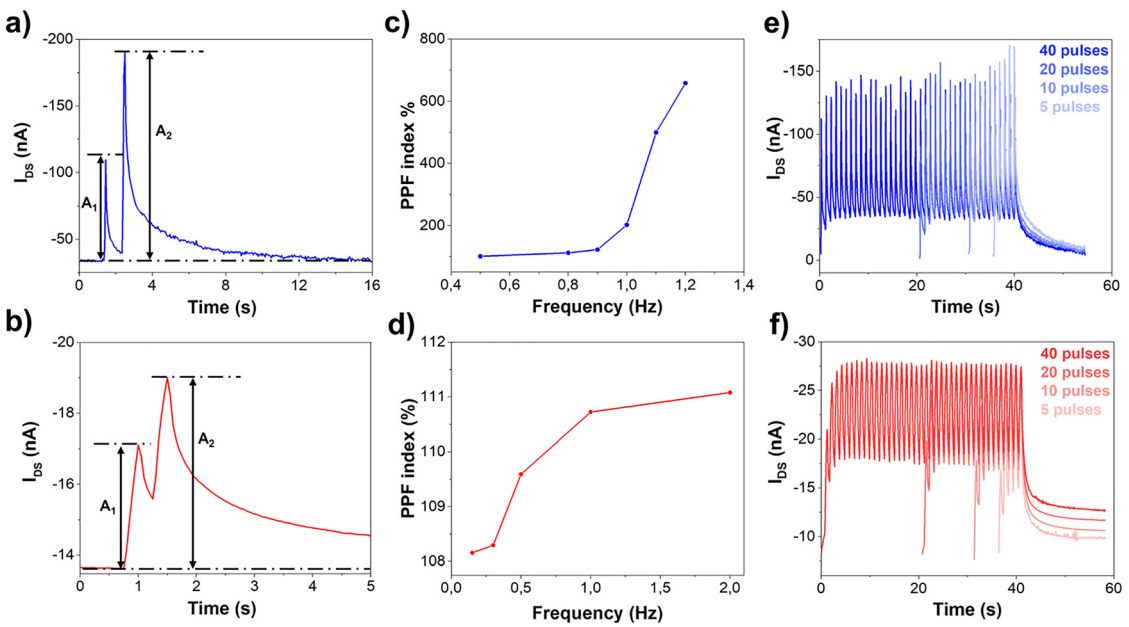

Fig. 3 PPF stimulated by (a) blue and (b) NIR light pulses (with a light intensity of 1 mW cm^{-2}, a frequency of 1 Hz and a time interval Δt of 1 s). The PPF change of OPST as a function of the pre-synaptic light pulse frequency of (c) blue and (d) NIR light pulses. Modulation of the I_{ds} current of the OPST under pulsed optical stimulation with 5, 10, 20, and 40 light pulses, at a pulse frequency of 1 Hz and an illumination power density of 1 mW cm^{-2}, in the blue range (e) and NIR range (f).

Specifically, the residual I_{ds} channel current increases from 9.8 to 12.7 nA when the number of light pulses increases from 5 to 40.

The signal facilitation and STP/LTP behavior of the OPST upon optical pulsed stimulation in the different spectral ranges are strictly correlated with the use of a photoactive BHJ comprising PyPBTM as the electron acceptor and the electron-trapping moiety. It has been already demonstrated in the literature that trapping of photogenerated charges in the active layer of OPTs (by oxygen-mediated formation of photo-induced radicals) can promote a synaptic-like behavior under optical stimulation.[43,65] In addition, we have recently demonstrated that the increase of charge recombination efficiency in OLETs when open-shell radicals are used as emissive molecules is strictly correlated with their capability of trapping electrons in the recombination layer.[51]

In order to further comprehend the dependency of the synaptic behavior of the OPST on the different spectral range of the optical stimulation and correlate it with the energetic distribution of the molecular orbitals of PyPBTM (and DPP-DTT), we investigated all of the photophysical processes involved in the photoexcitation of the BHJ by multilevel atomistic simulations (please see the Methods section for all technical details of the simulations).[66–69] The results are schematized in Fig. 4. Optical stimulation of the OPST by illumination in the NIR range

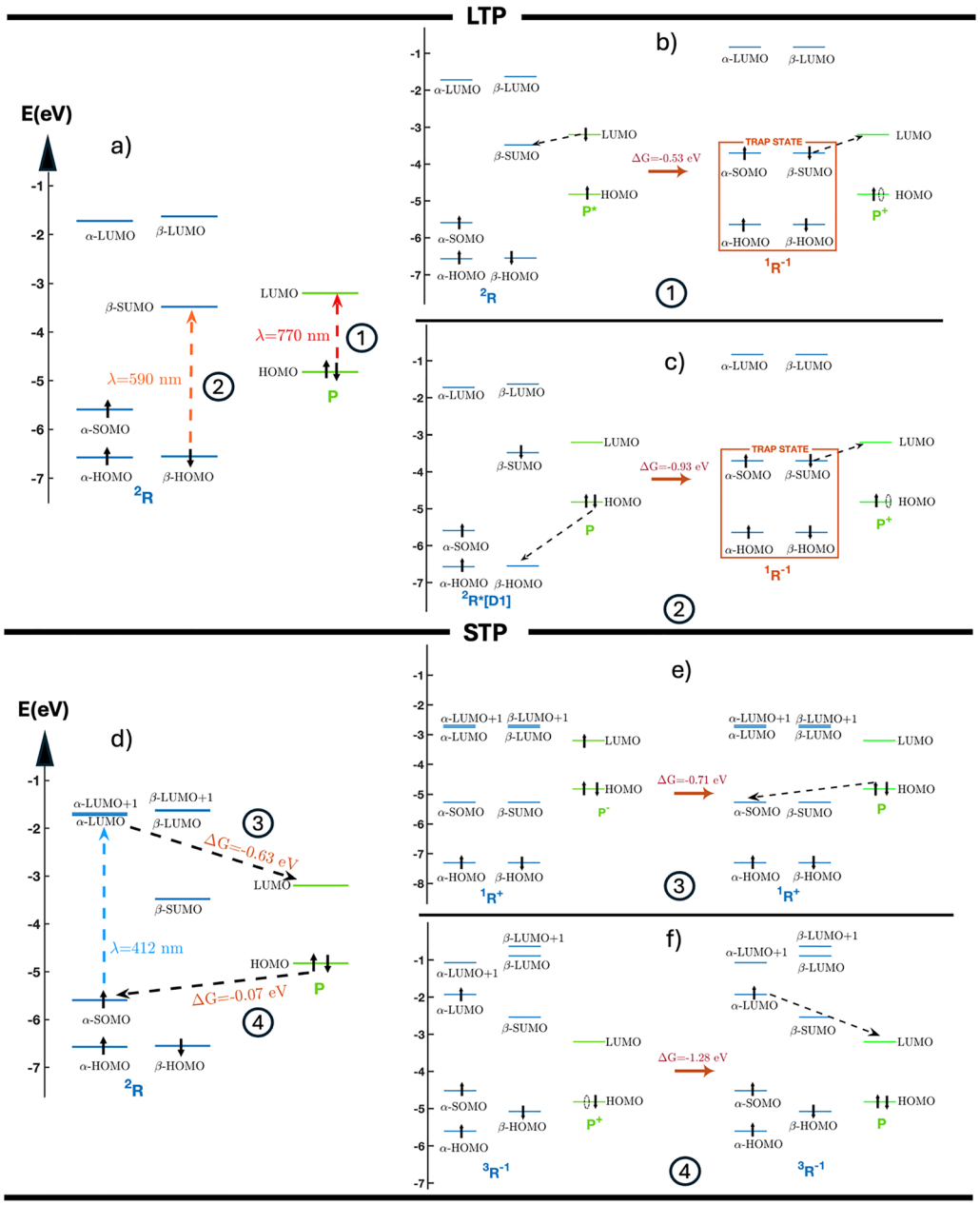

Fig. 4 Charge migration and decay mechanisms occurring in the PyPBTM:DPP-DTT system once light excitation is on and off in the NIR/yellow (a–c) and blue (d–f) spectral regions. Free energy differences related to charge-migration steps are shown in red.

corresponds to the excitation of DPP-DTT to its first singlet P* excited state (Fig. 4a). The photoexcited electron of DPP-DTT can be favorably transferred to the unoccupied β-SUMO of the neutral doublet radical (^{2}R) PyPBTM (process favored by −0.53 eV, Fig. 4b). Such transfer lowers by 0.12 eV the energy of the β-SUMO and induces its pairing with the α-SOMO electron, with the formation of a closed shell anion ($^1R^-$), letting back a mobile hole in the DPP-DTT cation (P^+). The mobile hole in DPP-DTT can diffuse to the HTL in the OPST and contribute to the photocurrent. As a consequence of electron transfer, the $^1R^-$ state becomes a trap, with the trapped electron in the β-SUMO now blocked at an energy 0.50 eV lower than that of the DPP-DTT LUMO, where it can slowly decay through recombination with a mobile hole, as experimentally demonstrated by the LPT characteristic shown in Fig. 3f. A similar behavior can also be triggered by photostimulation in the yellow region, which promotes the excitation of the neutral doublet radical (^{2}R) to its first doublet (D_1) excited state through a β-HOMO → β-SUMO transition (Fig. S1). This excited state can evolve by the energetically favored transfer of one electron from the spin-insensitive HOMO of DPP-DTT to the currently unoccupied β-HOMO of the excited radical (process favored by −0.93 eV) (Fig. 4c), yielding again a mobile hole in DPP-DTT and a closed shell anion ($^1R^-$) acting as a trap, which would be compatible with LPT characteristics.

On the other hand, when the system is optically excited in the blue spectral range, its evolution is incompatible with a LTP behavior. Stimulation in the blue region induces the excitation of (^{2}R) to the excited state ^{2}R* in radical sites which is a convolution of the α-SOMO → α-LUMO and α-SOMO → α-LUMO+1 electronic transitions (Fig. S1). Two complementary decay paths to the ground state can be identified which are based on energetically favored, two-step electron exchange Dexter mechanisms (Fig. 4d). The former path involves a first, favored (−0.63 eV) transfer of the excited electron from the α-LUMO/α-LUMO+1 states to the DPP-DTT LUMO, where it eventually recombines with majority carriers, letting back a closed shell PyPBTM cation ($^1R^+$). Such a reactive species can favorably (−0.71 eV) capture one electron from the DPP-DTT HOMO and accommodate it in its unoccupied α-SOMO to reform the ground state ^{2}R PyPBTM, injecting a mobile hole in the polymer (Fig. 4e). Alternatively, the latter path involves the energetically favored transfer of one electron from the spin insensitive HOMO of DPP-DTT to the currently unoccupied α-SOMO (process favored by −0.07 eV), yielding a mobile hole in DPP-DTT and a triplet-state anion ($^3R^-$). $^3R^-$ is a highly reactive species that can decay rapidly and transfer one electron to the DPP-DTT LUMO (process favored by −1.28 eV), where it is fated to recombine with majority carriers. A possible $^3R^-$ → $^1R^-$ intersystem conversion is ruled out because it is spin-forbidden and therefore slow and thus is unfavored and incompatible with a STP mechanism.

Overall, theoretical calculations fully support the experimental measurements on the optical pulsed stimulation of the OPST, indicating that much-faster electron recombination processes are activated in the case of blue-light stimulation involving the high-energy excitation of PyPBTM, because they bypass the formation of a metastable and slowly decaying $^1R^-$ trap state at the open-shell PyPBTM sites. This result is in very good agreement with the STP characteristic of the synaptic OPST when the blue-light stimulation protocol is applied. On the other hand, direct optical stimulation of the DPP-DTT donor component of the BHJ in the NIR spectral range is compatible with LTP characteristics.

In order to experimentally corroborate the theoretical picture of the stringent correlation between the peculiar energy-level and spin-multiplicity landscape of the DPP-DTT and PyPBTM BHJ with the different light-stimulated plasticity of the neuromorphic OPST, we optically excited the device with yellow light (580–600 nm), matching the low-energy excitation of PyPBTM (Fig. S1), *i.e.* excitation of the neutral doublet radical (^{2}R) to its first doublet (D_1) excited state through a β-HOMO → β-SUMO transition. Indeed, this mechanism is compatible with the LTP characteristic as predicted by the multilevel atomistic simulations: Fig. S4 shows the increase of persistent current of the OPST as the number of yellow-light pulses increases from 10 to 40 which is the experimental demonstration of the LTP behavior of the device.

To test the potential multi-mode operation of the OPST, sequential electrical stimulation (V_{gs} pulses) and optical stimulation (light pulses) were applied to the OPST, and the transient I_{ds} current was collected (Fig. 5a). Without electrical stimulation, the application of a single light pulse in the blue range (pulse duration: 1 s) causes a transient increase of the I_{ds} current, which returns to the initial value under dark conditions when the optical pulse is turned off (step 1). Instead, applying an electrical stimulus consisting of 5 voltage pulses at the gate electrode with V_{gs} being changed from 0 V to −6 V at 1 Hz (step 2) before the application of an optical stimulus consisting of single 1-second long pulse in the blue range (step 3), higher I_{ds} current is collected during optical stimulus with respect to step 1 (*i.e.* increase of 96 nA) which is correlated with the electrically induced facilitation. When the blue light is switched off, the I_{ds} current decays and eventually reaches a plateau. The persistent channel current (step 4) is 65 nA higher than the initial value achieved after step 1. This result confirms that the electrical inputs, when sequentially coupled with the blue optical inputs, can be used to enable LTP in OPST. Notably, the information stored in the device is erased by applying a positive V_{gs} bias (*i.e.* 14 V for 10 s, step 5): the channel current returns to the initial value in about 10 s and the LTP of the OPST is cancelled. Once LTP is erased, the device response to the optical stimulation during step 6 becomes equal to the response observed in step 1. Increasing the number of pulses in the electrical stimulation from 5 to 10 (step 7) results in a more intense facilitation, as indicated by the higher channel current reached during the optical stimulation in the blue range (step 8). As a consequence, the persistent channel current registered when the optical stimulation is switched off (step 9) is further increased up to 203 nA with respect to the value reached after the 5-pulse electrical stimulation.

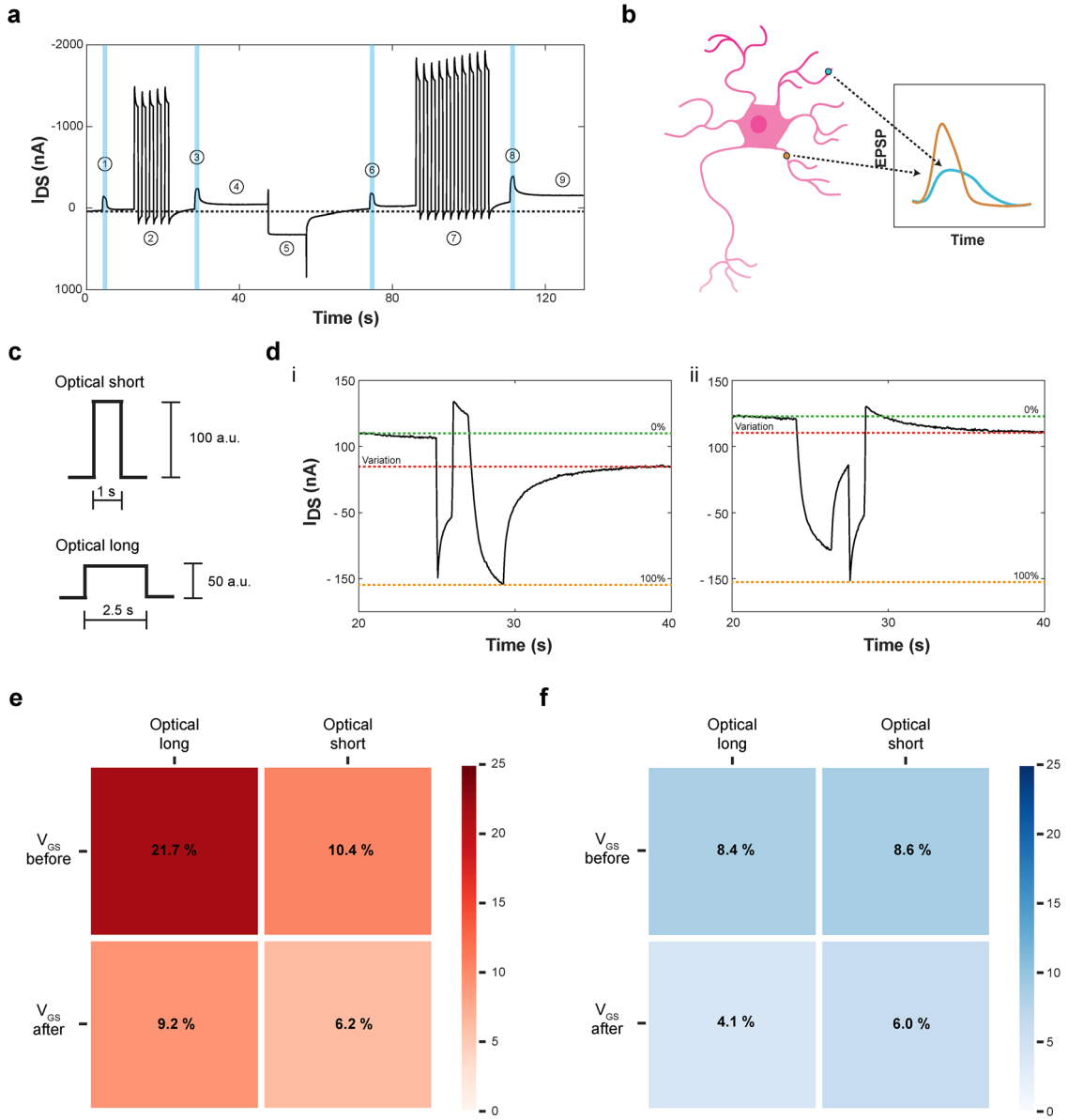

Fig. 5 (a) Facilitation of the I_{ds} current in the OPST in response to different stimulation sequences of electrical and optical stimuli: pristine polarization state (step 1), partial polarization (steps 2–4) by applying 5 voltages pulses at the gate electrode, erasing (step 5) and polarization by applying 10 voltage pulses at the gate electrode (steps 7–9). Optical stimuli are indicated with blue lines. (b) Schematic dendritic signal processing where excitatory postsynaptic potentials (EPSPs) change in shape due to different distances from the soma. (c) Schematics of the different optical input signals (0.4 and 1 mW cm^{-2}, respectively) used to register the response reported in panel (d), simulating EPSP changes in shape. (d) Registered channel current after the stimulation protocol combining long optical pulses in the NIR range and the voltage pulse: stimulation corresponding to the voltage pulse before the optical pulse (i) and to the optical pulse before the voltage pulse (ii); the variation in current is evaluated as percentage between the starting and maximum values. (e) Pattern recognition based on channel current variation in the OPST by combining long or short NIR optical stimulus and voltage stimulus (applied before or after the optical stimulus). (f) Pattern recognition based on the channel current variation in the OPST by combining long or short blue optical stimulus and voltage stimulus (applied before or after the optical stimulus).

Given the above results, the possibility of recapitulating dendritic computation with the OPST was explored. Interestingly, when engaged in a synaptic event, dendrites act like transmission lines, slightly dissipating the incoming stimuli that travel from the dendritic spines to the cell body.[34] As a consequence, neurons are able to discriminate between different incoming stimuli in space and time, as the shape of the stimulus is changed by dendritic integration, laying foundation for pattern recognition and spatio-temporal classification at a single-cell level. Such mechanisms fall under the name of Rall Cable Theory,[70] where an incoming stimulus is attenuated when received far away from the soma (Fig. 5b, blue line), with respect to a signal received in proximity to the cell body (Fig. 5b, orange line). A similar signal attenuation can also be observed based on the direction of the stimulus (from or to the soma).[71] In order to emulate such behavior, two different optical stimuli

were applied to the OPST (Fig. 5c). In particular, a short and strong optical stimulus (optical short) emulates a synaptic signal that instantaneously reaches the cell body, while a longer but weaker signal (optical long) emulates a synaptic signal that travels along a dendrite to reach the cell body. Such stimuli were deployed with both blue and NIR light stimulation. In addition, a square voltage pulse at the gate electrode (V_{gs} = −8 V, 1 s long) was applied either before or after the application of the light stimulus.

8 different combinations of stimuli were applied by changing all of the involved variables, *i.e.* long and short optical signals, applied either before or after the electrical stimulation and using both blue and NIR lights, while monitoring the channel current of the OPST. An exemplary measurement (long stimulus with NIR light, before and after the V_{gs} bias application) is shown in Fig. 5d. In order to assess the ability of the device to classify different patterns and signals, the variation of the baseline current (Fig. 5d, red line) was computed as a percentage change, where 0% is the value before the application of any stimulus (Fig. 5d, green line), while 100% is represented by the peak reached during the stimulation (Fig. 5d, yellow line). Fig. 5e shows the results of all combinations of signals, while employing NIR light. Notably, a significant difference can be observed in channel current variation between short and long optical stimulations, independent of the electrical stimulus (*i.e.*, moving along a row). In the same way, when moving along a column, it is possible to discern between the variations induced by an electrical stimulus applied before or after the optical one. Therefore, when employing NIR light, the OPST can discern between the two shapes of an optical signal, emulating dendrites. In addition, pattern classification is achieved, as the current variation depends on the order by which the electrical and optical stimuli are provided.

Even though the pattern recognition here demonstrated is limited to the temporal coincidence of solely two stimuli (optical and electrical), it remains relevant in terms of dendritic computation emulation, as dendrites were shown to execute temporal coincidence detection between just two stimuli (local excitatory synaptic inputs and backpropagating calcium spikes).[72]

Likewise, Fig. 5f shows the current variation when employing blue light. Notably, the OPST cannot correctly emulate dendritic integration features, as there is no significant difference when changing the duration of the optical stimulus (moving along rows). Such a result may be ascribed to the inadequacy of blue light to trigger LTP, as previously discussed.

Nonetheless, as the application of electrical pulses favored charge retention, a significant difference in current variation is observed when applying the optical stimulus before or after the electrical one. Therefore, even if the OPST cannot emulate dendritic computation when subjected to blue light, the interplay between electrical and optical stimuli enables pattern classification. When compared with other organic or inorganic device materials and architectures in photonic synaptic transistors (Table S1), the inherent multifunctionality and energy/spin configuration of the class of PyPBTM-based radicals allow long-lasting responsiveness for multiple-input stimulation which forms the basis for accurate pattern recognition.

Conclusions

We have developed a multi-mode solution-processed OPST capable of performing dendrite-like neuromorphic functions by both electrical and multi-color light stimulations and their combination. The molecular design-based innovative integration in a single transistor device of a ferroelectric dielectric and of a photoactive BHJ based on charge-trapping organic persistent radicals enables not only the essential synaptic functions such as STP and LPT but also the emulation of dendritic computation. In particular, the peculiar energy-level and spin-multiplicity landscape of the BHJ, comprising the DPP-DTT polymer as the electron donor and the PyPBTM persistent radical as the electron acceptor, allowed only STP under blue-light stimulation and STP and LTP under NIR-light stimulation. We demonstrate by theoretical calculations that the long-term plasticity displayed by the device was correlated with not only the neat generation of photo-induced holes in the donor component but also with the efficient formation of trap $^1R^-$ states in the radical component of the BHJ when specific photophysical pathways were activated by NIR- and yellow-light stimulation. Moreover, the multi-mode operation of the OPST enables long-lasting polarization in the ferroelectric dielectric layer by electrically pulsing at the gate electrode which can be synergically coupled with blue-light stimulation to obtain LTP. The as-engineered OPST can be considered as a prototypal transistor device to simulate parallel learning and dendrite integration since it can be operated by multiple-variable input stimuli combining and differentiating electrical and multicolor optical stimulations (*i.e.* blue and NIR light). Indeed, OPSTs can recognize and classify patterns among a basis of 8 different combinations of stimuli generated by changing all the electrical and optical variables: specifically, devices subject to a NIR-light stimulation protocol can discern between the two shapes of an optical signal, thus emulating cell dendrites.

The new class of OPSTs based on the use of persistent organic radicals are expected to be innovative components for AVSs for the capability to emulate (i) synapses with both STP and LTP (that forms the basis for learning and memory) and dendritic computation. Moreover, the inherent multifunctionality of the persistent organic radicals that we have recently demonstrated in the realization of high quantum efficiency OLETs[51] and high photosensitivity OPTs[52] can contribute to the fabrication of intelligent displays where light detection, light emission and neuromorphic characteristics should be integrated in a single device in order to realize the full-scene realistic display with high efficiency and low-power consumption.

Methods

Device fabrication

DPP-DTT was purchased from BOC Sciences. PyPBTM was synthesized according to the published procedure.[58] PVDF–TrFE–CFE

(70 : 30 : 8.5) was purchased from Arkema. C6Si (51 wt%) and organic solvents (cyclopentanone, chloroform and chlorobenzene) were purchased from Sigma Aldrich. Crosslinked DPP-DTT solution was prepared by dissolving DPP-DTT in chlorobenzene at a concentration of 4 mg mL^{-1} followed by the addition of 3.2 μL mL^{-1} C6Si solution. DPP-DTT : PyPBTM solution was prepared at a 1 : 3 weight ratio with chloroform. P(VDF–TrFE–CFE) (70 : 30 : 8.5) was dissolved in cyclopentanone (7 wt%). All chemicals were used as received without further purification.

OPSTs were fabricated in a bottom-gate/middle-contact configuration onto glass/ITO 25 mm × 25 mm substrates with a channel length of 100 μm and a channel width of 5000 μm. Substrates were cleaned in an ultrasonic bath twice with acetone and once with 2-propanol. Then the substrates were subjected to surface treatment with oxygen plasma prior to dielectric layer deposition. PVDF–TrFE–CFE solution was filtered using a 0.45 μm PTFE filter and deposited by spin-coating followed by an annealing process at 110 °C for 30 minutes under an inert atmosphere. Crosslinked DPP-DTT:C6Si solution was spin-coated in a glovebox and the substrates were exposed to air for 1 hour immediately after the deposition step. Then they were brought back into the glovebox and annealed at 90 °C overnight and finally at 200 °C for 10 minutes. 70 nm thick silver source/drain electrodes were deposited by thermal evaporation. DPP-DTT:PyPBTM solution was filtered using a 0.45 μm PTFE filter and deposited by spin-coating followed by an annealing process at 135 °C for 10 minutes under an inert atmosphere. Reference OFETs were fabricated following the same protocol as the OPSTs, but without the deposition of the DPP-DTT:PyPBTM photoactive layer.

Device optoelectronic characterization

UV-vis absorption spectra of the DPP-DTT:PyPBTM 100 nm thick film were obtained using a Jasco V-550 UV/vis spectrophotometer.

Electrical characterization studies of OPSTs were performed using a commercial platform (ARKEO, Cicci Research, Italy). Independent SMUs were controlled to supply drain and/or gate biases, with respect to the source electrode. Static characteristics were recorded by sweeping the gate voltage (−30 to +15 V), while keeping the drain electrode at a constant bias (−8 V) under both dark conditions and light excitation. Different exciting wavelengths were applied using the same commercial platform (ARKEO, Cicci Research, Italy), which allowed us to drive LEDs while operating different SMUs.

Pulsed electrical measurements were performed by fixing the drain bias with respect to the source, while applying square voltage pulses at the gate electrode, with desired amplitude and frequency. NIR, blue and yellow light pulses were applied while maintaining the gate voltage bias at 0 V and the drain voltage bias at −8 V with respect to the source electrode.

Computational analysis

Atomistic simulations of PyPBTM and DPP-DTT were carried out using a multi-level approach. The most stable conformers of the investigated molecules and polymers (treated as oligomers) were individuated using a conformer-rotamer ensemble sampling tool (CREST) algorithm[67] based on the GFN2-*x*TB tight-binding Hamiltonian for the search of the lowest energy configurations.[68,69] Then, the electronic and optical properties of the molecules were investigated using (time-dependent) density functional theory (TDDFT) simulations performed in a GTO framework by using the ORCA suite of programs.[66] Kohn–Sham orbitals were expanded on an all-electron def2-TZVPP Gaussian-type basis set.[73] The corresponding def2/J basis set was also used as an auxiliary basis set for Coulomb fitting in a resolution-of-identity/chain-of-spheres (RIJCOSX) framework.[74] Molecular geometries were fully optimized and their properties investigated by using the B3LYP functional,[75] with the addition of the pairwise D3 correction for the calculation of dispersion forces.[76] The absorption spectrum of PyPBTM was calculated using a time-dependent density functional theory approach at the same B3LYP@def2-TZVPP level of theory. A large basis set of 600 vectors connecting occupied and unoccupied Kohn–Sham orbitals was used to build the Davidson expansion space for the calculation of the first 30 electronic transitions of the molecule. An alternative strategy was used to calculate the absorption spectrum of the large DPP-DTT tetramer, using a simplified sTDDFT approach,[77,78] together with the CAM-B3LYP functional and the same def2-TZVPP basis set. PyPBTM and DPP-DTT and their positive and negative ions were embedded in an implicit $CHCl_3$ solvent using a conductor-like polarizable continuum model (CPCM) to calculate electronic and solvation energies.[79] The thermochemical properties of the same molecules were calculated at the B3LYP@def2-SVP level of theory.

Author contributions

G. B. and F. R. designed, fabricated and contributed to the optoelectronic characterization of the synaptic phototransistors, analysed the collected data, and contributed to writing the manuscript; U. B. contributed to the optoelectronic characterization of the OPSTs and designed and performed the experimental protocol for neuromorphic characterization of OPSTs, analysed the collected data, and contributed to writing the manuscript; G. B., F. R. and U. B. equally contributed to the manuscript; F. P. and G. M. performed the computational analysis for the description of the photophysical properties of the persistent radical-based blend and contributed to writing the manuscript; S. M. and L. B. provided the persistent radical compound and contributed to the protocol of processing; M. P. and M. B. discussed the data collected from the optoelectronic and neuromorphic characterization of the OPSTs and revised the manuscript; S. T. and F. S. conceived the concept and the use of the OPSTs, defined the experimental setup, and wrote and revised the manuscript; S. T. is responsible for the funding; S. T. and F. S. are the corresponding authors.

Conflicts of interest

There are no conflicts to declare.

Data availability

Data analysis was carried out using custom Python scripts, based on open libraries such as NumPy and SciPy. No data repository was created for this work. Data analysis scripts and raw data are available upon request.

Supplementary information (SI) is available. See DOI: https://doi.org/10.1039/d5mh01710f.

Acknowledgements

The authors thank Federico Prescimone for the technical support. This work was supported by the project ''MULTIRADICALS4LIGHT: Design, synthesis, and characterization of inert MULTIfunctional diRADICALoidS for organic LIGHT-emitting transistors'' funded by the MIUR Progetti di Ricerca di Rilevante Interesse Nazionale (PRIN) – 202253P3YJ_PE5_PRIN2022. The work of F. P. and G. M. has been financially supported by ICSC-Centro Nazionale di Ricerca in High Performance Computing, Big Data, and Quantum Computing, funded by European Union-NextGenerationEU (Grant No. CN00000013), and by the Italian Minister of the University and Research (MUR) within the PRIN-2022 research program (project ''NIR+,'' Grant No. 2022BREBFN).

References

1 C. Mead, *Proc. IEEE*, 1990, **78**, 1629–1636.
2 S. Dai, Y. Zhao, Y. Wang, J. Zhang, L. Fang, S. Jin, Y. Shao and J. Huang, *Adv. Funct. Mater.*, 2019, **29**, 1903700.
3 P. Yao, H. Wu, B. Gao, J. Tang, Q. Zhang, W. Zhang, J. J. Yang and H. Qian, *Nature*, 2020, **577**, 641–646.
4 H. Han, H. Yu, H. Wei, J. Gong and W. Xu, *Small*, 2019, **15**, 1900695.
5 H. Tan, Q. Tao, I. Pande, S. Majumdar, F. Liu, Y. Zhou, P. O. Å. Persson, J. Rosen and S. van Dijken, *Nat. Commun.*, 2020, **11**, 1369.
6 Y. Zhou and S. Ramanathan, *Proc. IEEE*, 2015, **103**, 1289–1310.
7 C. Mead, *Nat. Electron.*, 2020, **3**, 434–435.
8 N. Lepri, A. Glukhov, L. Cattaneo, M. Farronato, P. Mannocci and D. Ielmini, *IEEE J. Electron Devices Soc.*, 2023, **11**, 587–601.
9 J. Y. Gerasimov, D. Tu, V. Hitaishi, P. C. Harikesh, C. Yang, T. Abrahamsson, M. Rad, M. J. Donahue, M. S. Ejneby and M. Berggren, *Adv. Sci.*, 2023, **10**, 2207023.
10 E. R. W. Van Doremaele, X. Ji, J. Rivnay and Y. Van De Burgt, *Nat. Electron.*, 2023, **6**, 765–770.
11 I. Krauhausen, C. Coen, S. Spolaor, P. Gkoupidenis and Y. van de Burgt, *Adv. Funct. Mater.*, 2024, **34**, 2307729.
12 U. Bruno, D. Rana, C. Ausilio, A. Mariano, O. Bettucci, S. Musall, C. Lubrano and F. Santoro, *Mater. Horiz.*, 2024, **11**, 2865–2874.
13 G. M. Matrone, U. Bruno, C. Forró, C. Lubrano, S. Cinti, Y. van de Burgt and F. Santoro, *Adv. Mater. Technol.*, 2023, **8**, 2201911.
14 N. Spruston, Y. Schiller, G. Stuart and B. Sakmann, *Science*, 1995, **268**, 297–300.
15 E. R. Kandel, *Principles of neural science*, 2000, vol. 4, pp. 381–403.
16 L. F. Abbott and S. B. Nelson, *Nat. Neurosci.*, 2000, **3**, 1178–1183.
17 T. Ohno, T. Hasegawa, T. Tsuruoka, K. Terabe, J. K. Gimzewski and M. Aono, *Nat. Mater.*, 2011, **10**, 591–595.
18 M. K. Kim and J. S. Lee, *ACS Nano*, 2018, **12**, 1680–1687.
19 Y. He, L. Zhu, Y. Zhu, C. Chen, S. Jiang, R. Liu, Y. Shi and Q. Wan, *Adv. Intell. Syst.*, 2021, **3**, 2000210.
20 Y. He, Y. Yang, S. Nie, R. Liu and Q. Wan, *J. Mater. Chem. C*, 2018, **6**, 5336–5352.
21 Y. Nishitani, Y. Kaneko, M. Ueda, T. Morie and E. Fujii, *J. Appl. Phys.*, 2012, **111**, 124108.
22 S. W. Cho, S. M. Kwon, Y.-H. Kim and S. K. Park, *Adv. Intell. Syst.*, 2021, **3**, 2000162.
23 Y. Chen, H. Yu, J. Gong, M. Ma, H. Han, H. Wei and W. Xu, *Nanotechnology*, 2018, **30**, 012001.
24 P. C. Harikesh, C. Y. Yang, H. Y. Wu, S. Zhang, M. J. Donahue, A. S. Caravaca, J. Da Huang, P. S. Olofsson, M. Berggren, D. Tu and S. Fabiano, *Nat. Mater.*, 2023, **22**, 242–248.
25 T. Sarkar, K. Lieberth, A. Pavlou, T. Frank, V. Mailaender, I. McCulloch, P. W. M. Blom, F. Torricelli and P. Gkoupidenis, *Nat. Electron.*, 2022, **5**, 774–783.
26 J. Y. Gerasimov, D. Zhao, A. Sultana, T. Abrahamsson, S. Han, D. Bliman, D. Tu, D. T. Simon, R. Olsson, X. Crispin, M. Berggren and S. Fabiano, *Adv. Electron. Mater.*, 2021, **7**, 2001126.
27 P. Mannocci, M. Farronato, N. Lepri, L. Cattaneo, A. Glukhov, Z. Sun and D. Ielmini, *APL Mach. Learn.*, 2023, **1**, 010902.
28 U. Bruno, D. Rana, C. Ausilio, A. Mariano, O. Bettucci, S. Musall, C. Lubrano and F. Santoro, *Mater. Horiz.*, 2024, **11**, 2865–2874.
29 G. M. Matrone, U. Bruno, C. Forró, C. Lubrano, S. Cinti, Y. van de Burgt and F. Santoro, *Adv. Mater. Technol.*, 2023, **8**, 2201911.
30 A. Rubino, C. Livanelioglu, N. Qiao, M. Payvand and G. Indiveri, *IEEE Trans. Circuits Syst. I: Regul. Pap.*, 2021, **68**, 45–56.
31 K. Boahen, *Nature*, 2022, **612**, 43–50.
32 G. X. Ritter, L. Iancu and G. Urcid, LNCS 2905 – Neurons, Dendrites, and Pattern Classification, https://doi.org/10.1007/978-3-540-24586-5_1.
33 B. A. Bicknell and M. Häusser, *Neuron*, 2021, **109**, 4001–4017.
34 W. Rall, *J. Cell. Comp. Physiol.*, 1955, **46**, 373–411.
35 T. Euler, P. B. Detwiler and W. Denk, *Nature*, 2002, **418**, 845–852.
36 K. L. Briggman, M. Helmstaedter and W. Denk, *Nature*, 2011, **471**, 183–190.
37 Y. Guo, G. Yu and Y. Liu, *Adv. Mater.*, 2010, **22**, 4427–4447.
38 M. Prosa, E. Benvenuti, D. Kallweit, P. Pellacani, M. Toerker, M. Bolognesi, L. Lopez-Sanchez, V. Ragona, F. Marabelli and S. Toffanin, *Adv. Funct. Mater.*, 2021, **31**, 2104927.

39 M. Prosa, S. Moschetto, E. Benvenuti, M. Zambianchi, M. Muccini, M. Melucci and S. Toffanin, *J. Mater. Chem. C*, 2020, **8**, 15048–15066.
40 S. Moschetto, E. Benvenuti, H. Usta, R. Ozdemir, A. Facchetti, M. Muccini, M. Prosa and S. Toffanin, *Adv. Mater. Interfaces*, 2022, **9**, 2101926.
41 G. Baroni, F. Reginato, M. Prosa, M. Brucale, F. Prescimone, M. Seri, K. Gallegos-Rosas, C. Soldano, M. Bolognesi and S. Toffanin, *J. Mater. Chem. C*, 2024, **12**, 12962–12970.
42 Y. Ren, L. Sun, Y. Xie, S. Gao, Y. Du, M. Zhang, X. Wu, X. Zhu, F. Yang and W. Hu, *J. Mater. Chem. C*, 2024, **12**, 9455.
43 R. Jia, X. Wu, W. Deng, X. Zhang, L. Huang, K. Niu, L. Chi and J. Jie, *Adv. Funct. Mater.*, 2019, **29**, 1905657.
44 W.-C. Chen, Y.-S. Wu, Y.-C. Lin, Y.-H. Huang, J.-Y. Wu, K.-W. Lin, C.-L. Liu and W.-C. Chen, *Mater. Horiz.*, 2025, **12**, 8711–8723.
45 C.-H. Tsai, W.-C. Chen, Y.-C. Lin, Y.-H. Huang, K.-W. Lin, J.-Y. Wu, T. Satoh, W.-C. Chen and C.-C. Kuo, *Small*, 2024, **20**, 2402567.
46 K. Lee, H. Han, Y. Kim, J. Park, S. Jang, H. Lee, S. W. Lee, H. Kim, Y. Kim and T. Kim, *Adv. Funct. Mater.*, 2021, **31**, 2105596.
47 M. K. Kim and J. S. Lee, *Adv. Mater.*, 2020, **32**, 1907826.
48 Y. Li, G. He, W. Wang, C. Fu, S. Jiang, E. Fortunato and R. Martins, *Mater. Horiz.*, 2024, **11**, 3867.
49 Y. Liu, Z. Yin, C. Liu, Z. Liu, S. Liu and Q. Zheng, *Chem. Eng. J.*, 2025, **507**, 160538.
50 Z. X. Chen, Y. Li and F. Huang, *Chem*, 2021, **7**, 288–332.
51 F. Reginato, E. Lunedei, S. Mattiello, G. Baroni, M. Bolognesi, F. Porcelli, G. Mattioli, Y. Hattori, M. Prosa, L. Beverina and S. Toffanin, *Adv. Funct. Mater.*, 2024, **35**, 2411845.
52 G. Baroni, F. Reginato, S. Mattiello, S. Moschetto, M. Prosa, M. Bolognesi, L. Beverina and S. Toffanin, *ACS Appl. Electron. Mater.*, 2025, **7**, 3694–3703.
53 S.-M. Yoon, S. Yang, S.-W. Jung, C.-W. Byun, M.-K. Ryu, W.-S. Cheong, B. Kim, H. Oh, S.-H. Ko Park and C.-S. Hwang, *Appl. Phys. A*, 2011, **102**, 983–990.
54 S.-Y. Wu, *IEEE Trans. Electron Devices*, 1974, **21**, 499–504.
55 C. Wang, A. Agrawal, E. Yu and K. Roy, *Front. Neurosci.*, 2021, **15**, 661667.
56 C. Park, K. Lee, M. Koo and C. Park, *Adv. Mater.*, 2021, **33**, 2004999.
57 X. Chen, L. Liu, S. Z. Liu, Y. S. Cui, X. Z. Chen, H. X. Ge and Q. D. Shen, *Appl. Phys. Lett.*, 2013, **102**, 063103.
58 S. Mattiello, F. Corsini, S. Mecca, M. Sassi, R. Ruffo, G. Mattioli, Y. Hattori, T. Kusamoto, G. Griffini and L. Beverina, *Mater. Adv.*, 2021, **2**, 7369–7378.
59 D. Liu, J. Zhang, Q. Shi, T. Sun, Y. Xu, L. Li, L. Tian, L. Xiong, J. Zhang and J. Huang, *Adv. Mater.*, 2024, **36**, 2305370.
60 Y. Wu, S. Dai, X. Liu, P. Guo, J. Zhang, T. Sun, Z. Guo, Y. Xu, H. Liang and L. Xiong, *Adv. Funct. Mater.*, 2024, **34**, 2315175.
61 H. Wang, Q. Zhao, Z. Ni, Q. Li, H. Liu, Y. Yang, L. Wang, Y. Ran, Y. Guo, W. Hu and Y. Liu, *Adv. Mater.*, 2018, **30**, 1803961.
62 R. A. John, J. Ko, M. R. Kulkarni, N. Tiwari, N. A. Chien, N. G. Ing, W. L. Leong and N. Mathews, *Small*, 2017, **13**, 1701193.
63 L. Yin, W. Huang, R. Xiao, W. Peng, Y. Zhu, Y. Zhang, X. Pi and D. Yang, *Nano Lett.*, 2020, **20**, 3378–3387.
64 J. Zhang, Y. Lu, S. Dai, R. Wang, D. Hao, S. Zhang, L. Xiong and J. Huang, *Research*, 2021, **2021**, 7131895.
65 Q. Wang, J. Yang, S. Braun, M. Fahlman and X. Liu, *Org. Electron.*, 2022, **100**, 106375.
66 F. Neese, *Wiley Interdiscip. Rev.: Comput. Mol. Sci.*, 2012, **2**, 73–78.
67 P. Pracht, F. Bohle and S. Grimme, *Phys. Chem. Chem. Phys.*, 2020, **22**, 7169–7192.
68 C. Bannwarth, S. Ehlert and S. Grimme, *J. Chem. Theory Comput.*, 2019, **15**, 1652–1671.
69 S. Grimme, *J. Chem. Theory Comput.*, 2019, **15**, 2847–2862.
70 H. Cuntz, M. W. H. Remme and B. Torben-Nielsen, *The Computing Dendrite*, Springer Series in Computational Neuroscience, 2014, vol. 11.
71 R. Wilfrid, *The Theoretical Foundation of Dendritic Function*, The MIT Press, 1994.
72 A. Reyes, *Annu. Rev. Neurosci.*, 2001, **24**, 653–675.
73 A. Schäfer, H. Horn and R. Ahlrichs, *J. Chem. Phys.*, 1992, **97**, 2571–2577.
74 F. Neese, F. Wennmohs, A. Hansen and U. Becker, *Chem. Phys.*, 2009, **356**, 98–109.
75 A. D. Becke, *J. Chem. Phys.*, 1992, **96**, 2155–2160.
76 S. Grimme, J. Antony, S. Ehrlich and H. Krieg, *J. Chem. Phys.*, 2010, **132**, 154104.
77 S. Grimme, *J. Chem. Phys.*, 2013, **138**, 2013.
78 T. Risthaus, A. Hansen and S. Grimme, *Phys. Chem. Chem. Phys.*, 2014, **16**, 14408–14419.
79 V. Barone and M. Cossi, *J. Phys. Chem. A*, 1998, **102**, 1995–2001.